IEEE Access
Multidisciplinary | Rapid Review | Open Access Journal

Received 10 December 2024, accepted 2 January 2025, date of publication 7 January 2025, date of current version 13 January 2025.

Digital Object Identifier 10.1109/ACCESS.2025.3526752

RESEARCH ARTICLE

Operation of a Grid-Forming Converter Controlled by the Flux Vector

JUAN DOLADO FERNÁNDEZ[1], EDUARDO RAUSELL NAVARRO[2], JOSÉ LUIS RODRÍGUEZ AMENEDO[1], (Senior Member, IEEE), JOAQUÍN ELOY-GARCÍA[3], AND SANTIAGO ARNALTES GÓMEZ[1]

[1]Electrical Engineering Department, University Carlos III of Madrid, 28911 Madrid, Spain
[2]Department of Technology, Research Centre for Energy, Environment, and Technology (CIEMAT), 28040 Madrid, Spain
[3]Ingenia Power Solutions SL, 28918 Madrid, Spain

Corresponding author: Juan Dolado Fernández (jdolado@ing.uc3m.es)

This work was supported in part by the Ministerio de Ciencia e Innovación (MCIN)/Agencia Estatal de Investigación (AEI)/10.13039/501100011033 under Grant PDC2022-133349-I00, and in part by European Union "NextGenerationEU/Plan de Recuperación, Transformación y Resiliencia (PRTR)."

ABSTRACT The electric power system is undergoing a significant transition. Renewable energy generation capacity has increased, leading to the displacement of synchronous generators (SG) and a growing concern about grid stability due to the decrease of rotating inertial energy. Grid-forming (GFM) converters have become a technological solution to this challenge, as they are capable of operating in low strength system conditions and helping to stabilize the voltage and frequency of the grid. In this paper, a novel control scheme for GFM converters is validated in a commercial converter according to the National Grid ESO, called National Energy System Operator (NESO) since October 2024. The control scheme uses the flux vector as a simple and effective method for limiting the active and reactive currents without internal current loops. For this purpose, a hardware test bed has been implemented consisting of two DC sources emulating a photovoltaic (PV) plant which feed the DC bus a voltage source converter (VSC), a grid emulator which allows to generate the desired disturbances in the grid to evaluate the converter's response and a three-phase load. The results obtained have validated that these GFM converters based on the flux vector are capable of synchronizing with the grid, responding against frequency disturbances like phase jumps or faults in the grid and operating in islanded mode. In addition, the innovative method used to limit the active and reactive current has also been tested, comparing its performance with that of a conventional GFM scheme, showing an improvement in the response stability.

INDEX TERMS Grid-forming, flux vector, current limiter, national grid ESO.

LIST OF ABBREVIATIONS

SG	Synchronous Generator.
GFM	Grid-forming.
NESO	National Energy System Operator.
PV	Photovoltaic.
VSC	Voltage Source Converter.
IBR	Inverter-Based Resources.
ENTSOE-E	European Network of Transmission System Operators for Electricity.
GFL	Grid-following.
PLL	Phase-Locked Loop.
VOC	Virtual Oscillation-based Controller.
RCL	Reactive Control Loop.
CL	Current Limiter.
SCL	Synchronization Control Loop.
PSS	Power System Stabilizer.
FCL	Flux Control Loop.
PWM	Pulse Width Modulation.
ZOH	Zero-Order Hold.
IGBT	Insulated Gate Bipolar Transistors.
PPS	Pacific Power Source.

The associate editor coordinating the review of this manuscript and approving it for publication was Binit Lukose.

I. INTRODUCTION

The e need to reduce the impact of climate change has accelerated the energy transition to meet the increasing demand for carbon-neutral energy. Since 2013, the amount of renewable energy added to the grid each year has surpassed the total amount of nuclear and fossil fuels combined [1]. Most of these renewable energy resources, like PV or wind, use inverter-based resources (IBRs) to connect to the grid [2], [3].

Generation based on IBRs behaves differently from conventional generation based on synchronous generators (SGs), since inherently they are not capable of providing inertia and strength to the grid and also have a lower over current capacity. Consequently, and as the European Network of Transmission System Operators for Electricity (ENTSOE-E) recognizes, the electrical system is facing additional difficulties due to the transition from a centralized system based on SGs to a distributed system based on IBRs, becoming a weaker system [4].

Currently, the main control method currently used for IBRs is the grid-following (GFL) converters. These inverters use a current controller loop to manage the amount of current supplied to the grid and a phase-locked loop (PLL) for synchronization [5]. However, in low-strength systems, the control structure of GFLs may face instability issues [6], [7], since a minor disturbance can lead to significant fluctuations and deviations in grid frequency, potentially triggering the disconnection of low-frequency demand and, in extreme cases, the collapse of the power system [8], [9]. Furthermore, GFLs converters cannot neither operate in islanded mode nor contribute in the restoration of the system in case of blackout [10].

As a result, another control method for IBRs has emerged as an alternative to solve these issues: the grid-forming converters. Although currently most grid codes do not mention what a GFM is, it is a well-developed concept and even the minimum performance requirements for these converters appear in the grid code published by National Grid ESO for Great Britain [11].

The main objective of GFM converters is to maintain the internal voltage phasor through the control of the angle and amplitude of the voltage modulated by the inverter independently of the grid voltage or the load [10]. In fact, commonly the simple representation of a GFM converter is a voltage source with a small impedance in series and the representation of a GFL converter is a current source with a high impedance in parallel [12]. This is one of the major differences between these converters, since GFM are able to generate a voltage even in islanded mode while GFL need a grid voltage for synchronization and current injection.

Maintaining a constant voltage even in the presence of disturbances in the grid is of real interest for the decentralized grids that are currently being implemented with the inclusion of renewable energies. This type of IBRs are able to respond to network disturbances without losing their stability, being recommended for use in weak systems, for voltage and frequency stabilization, damping of power oscillations or blackstart restoration [13], [14].

In the literature, depending on their mode of operation, different types of GFM converters can be found. The first class is the simplest implementation and is based on droop controls [15], [16], [17], [18], [19]. This control technique replicates the govern action of SGs that enables the parallel operation of multiple IBRs. However, the absence of inertial response is one of its main disadvantages. The inertial and damping properties of SGs are included into the second class of GFM converters, known as synchronous-machine-based controllers [20], [21], [22], [23], [24], [25]. The third and last category is based on non-linear algorithms, such as the virtual oscillation-based (VOC) method [17], [25], [26], [27], [28]. This technique emulates the dynamics of a weakly non-linear oscillator by means of a single dead-zone oscillator which is composed by a virtual resistor, a capacitor, an inductor and a voltage-dependent current source [29].

An important element of the GFM converters is the current limiting technique. The current may exceed the nominal value during events such as a voltage faults or major grid disturbances and, unlike the SGs, power electronics can only handle small over currents (in the order of 1.1-1.3 p.u.) [30], [31]. According to the literature, three main strategies have been proposed to limit the current. The first one consists of adding saturators to the internal current control loops [32], however, this technique can provoke to instability in the system [33], [34]. The second method consists of switching to GFL control mode using a PLL during faults [35], [36], [37]. However, this method has stability problems in low-strength systems as mentioned above [6], [7]. Finally, the third strategy consists of using virtual impedances [38], [39]. In [40] the influence of the virtual impedance on the grid-forming control for current limitation is analyzed, where it is shown that the current limitation is largely depending on the fault location and the selected virtual impedance. In [41], it is also indicated how the tuning of the virtual impedance parameters is not very obvious. It has also been shown that the use of virtual impedances can lead to stability problems in parallel operation [42]. In addition, it has been demonstrated that the virtual impedance ratio has a contradictory effect on the system dynamics and the transient stability, i.e., a resistive virtual impedance results in a well-damped current response but a very limited transient stability margin, while an inductive virtual impedance results in a poorly-damped current response but an acceptable transient stability margin [43].

To solve these problems, a novel GFM control scheme is presented in this paper which proposes a simple and effective way to limit the active and reactive currents without internal current loops. The advantages and limitations of the proposed control technique and existing control methods are summarized in Table 1. To avoid high overcurrents during

TABLE 1. Comparison of different current-limiting control methods.

Current-Limiting Strategy	Advantages	Disadvantages
Add Saturators	Simple implementation	May cause loss of stability
Switch to GFL control	Good in steady-state	It is not advisable to change the control mode Can suffer from transient overcurrents During deep voltage dips the PLL may lose stability
Virtual Impedance	Good to restore normal operation Tradeoff between current limitation and stability [49]	Complex parameter setting Can suffer from transient overcurrents
Flux Vector Scheme	Simple implementation Good in steady-state Good to restore normal operation Internal current loops are eliminated	Can suffer from transient overcurrents

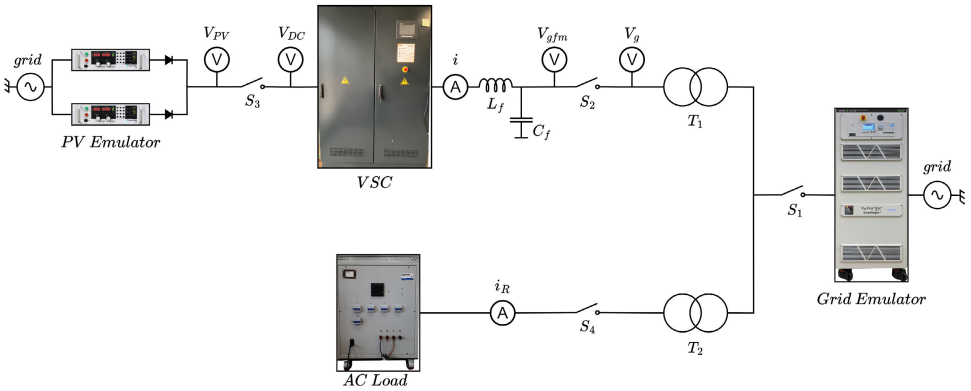

FIGURE 1. Test bed scheme.

transients, a protection maneuver has been implemented, which will be explained below.

This scheme presents an innovative solution that regulates a state variable, known as flux vector, obtained as the sum of the output current multiplied by the filter inductance plus the integral of the voltage measured at the converter terminals. In the past, this variable has been used to control inverters in microgrids [44] or to use direct or predictive controls [45], [46] but not for a grid-forming converter. In addition, this control system has been implemented in a commercial converter and the necessary capabilities established by the Great Britain grid code and in the document of National Grid ESO "Great Britain Grid Forming Best Practice Guide (April 2023)" [47], [48] have been verified on a power test bed.

The main contributions of this study are summarized as follows:

1) New control methodology for grid-forming converters without internal current loops.
2) New current limiting method without compromising system stability.
3) New method of synchronization with the grid based on the converter's flux vector.
4) Validation of the algorithm through a power loop in a laboratory with a commercial converter.
5) Compliance with the requirements currently required by National Grid ESO (Best practice guide for grid forming converters, 2023) for this type of converters controlled by the flux vector.

The article is structured as follows. The designed test bed scheme is described in Section II. A summary of the flux vector algorithm and the control scheme implemented are detailed in Section III and Section IV respectively. Section V shows a summary of the equipment used in the laboratory, the National Grid Requirements and the results obtained for the tests performed. Finally, Section VI presents main conclusions and future works to be developed.

II. TEST BED SCHEME

In order to replicate the tests established in [47], the scheme shown in Fig. 1 has been implemented in the laboratory. On the left side of Fig. 1, there are located two adjustable power supplies feeding the converter's DC bus voltage when the DC switch (S_3) is closed. Next is located the voltage source converter, its LC filter (L_f, C_f) and a switch to connect and disconnect the AC side of the converter (S_2) to the point of common coupling (PCC) through a transformer (T_1). In addition, through another transformer (T_2) and another switch (S_4) an adjustable three-phase resistive load can be

connected to the system. Finally, the grid emulator switch (S_1) is placed inside the equipment itself and has been used to validate the islanded mode operation of the converter by disconnecting the power source from the system in the middle of the test.

On the other hand, measuring devices are required for the operation of the control system. Inside the converter cabinet, several voltage sensors have been installed to measure at four different points. The first one measures the DC voltage of the PV Emulator (V_{PV}) and the second point measures the voltage in the DC bus capacitor (V_{DC}). On the AC side, the converter output voltages (V_{gfm}) and the grid voltages (V_g) of each phase have been measured. The currents in the converter's output filter (i) is also being measured. All these measurements are read by the interface board and sent to the control board. Finally, an oscilloscope DS1052E Rigol has been placed outside the converter to monitor the currents in the resistive load (i_R). The grid emulator also includes internal voltage and current measurements that can be monitored through its interface.

III. FLUX VECTOR ALGORITHM

According to the scheme shown in Fig. 1, the electrical equation at the converter's output can be expressed as

$$e = L_f \frac{di}{dt} + v_{gfm} \tag{1}$$

where e represents the internal voltage of the converter, L_f the filter inductance and v_{gfm} the output voltage of the converter. Furthermore, the grid voltage v_g can be expressed as a function of a flux vector λ at the PCC as follows

$$v_g = \frac{d\lambda}{dt} \tag{2}$$

If the converter is connected to the grid v_{gfm} and v_g are the same voltage and, therefore, substituting (2) into (1) the electrical equation can be expressed as

$$e = \frac{d}{dt}(L_f i + \lambda) \tag{3}$$

where the converter flux vector is defined as the derivative terms, resulting in

$$\lambda_v = L_f i + \lambda \tag{4}$$

Considering that v_{gfm} and v_g are equal and subtracting λ from (2) and substituting it in (4), the flux vector of the converter can be calculated as a function of the output current and voltage, yielding

$$\lambda_v = L_f i + \int v_{gfm}\, dt \tag{5}$$

In the model implemented in the laboratory, the converter's flux vector $\alpha\beta$ components ($\lambda_{\alpha v}$, $\lambda_{\beta v}$) are obtained as shown in Fig. 2 based on (5), where the frequency, f, has been set to 50 Hz and w_c at the high pass filter has been calculated for a cut-off frequency of 5 Hz. This filter is added in order to eliminate the continuous component that appears when

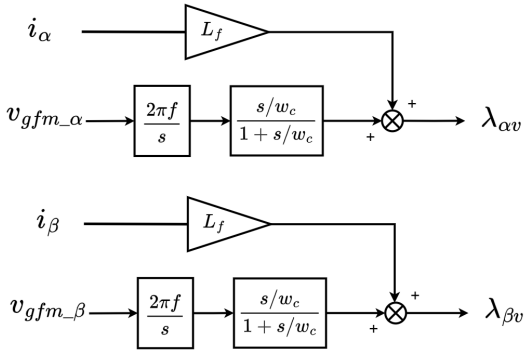

FIGURE 2. Converter flux vector measurement.

integrating the voltage. For the calculation of the grid flux, the same method has been implemented but eliminating the current term multiplied by the filter inductance complying with (2).

On the other hand, subtracting i from (4) and substituting in (3) results in

$$\frac{d\lambda_v}{dt} = e \tag{6}$$

Transforming the three-phase variables of (4), (6) and (2) into a vector space referred to a rotation dq axes rotating at ω rad/s, the dynamic equations can be obtained as

$$\vec{\lambda_v} = L_f \vec{i} + \vec{\lambda} \tag{7}$$

$$\frac{d\vec{\lambda_v}}{dt} + j\omega\vec{\lambda_v} = \vec{e} \tag{8}$$

$$\frac{d\vec{\lambda}}{dt} + j\omega\vec{\lambda} = \vec{v_g} \tag{9}$$

In steady state operation, v_{gfm} and v_g are the same voltage and the derivative terms of (7) and (8) can be cancelled, obtaining

$$\vec{e} = j\omega\vec{\lambda_v} \tag{10}$$

$$\vec{v_{gfm}} = j\omega\vec{\lambda} \tag{11}$$

Multiplying (7) by $j\omega$, yields

$$j\omega\vec{\lambda_v} = j\omega L_f \vec{i} + j\omega\vec{\lambda} \tag{12}$$

and substituting (10) and (11) in (12) results in

$$\vec{e} = j\omega L_f \vec{i} + \vec{v_{gfm}} \tag{13}$$

Therefore, the internal voltage of the converter is equal to the sum of the voltage drop in the inductance and the voltage at the terminals $\vec{v_{gfm}}$. The equivalent circuit that can be represented by this equation is analogous to that of a SG. Consequently, the active (P) and reactive (Q) powers can be obtained as

$$P = \frac{3}{2}\left(\frac{v_{gfm}}{j\omega L_f}\right) e\, sin\delta \tag{14}$$

$$Q = \frac{3}{2}\left(\frac{v_{gfm}}{j\omega L_f}\right)(e\, cos\delta - v_{gfm}) \tag{15}$$

where $j\omega L_f$ is the value of the reactance and δ is the angle between the internal voltage of the converter $\vec{e}$ and the terminal voltage $\vec{v_{gfm}}$. According to (10), the voltage $\vec{e}$ is proportional to the flux vector $\vec{\lambda_v}$, allowing its regulation to control the converter's active and reactive power.

IV. CONTROL SYSTEM DESCRIPTION

For the designed control system to operate properly, the measurements of the DC (V_{PV}, V_{DC}) and AC voltages (V_{gfm_abc}, V_{g_abc}) on both sides of the switches and the converter's output currents (i_{abc}) are required. Before connecting the converter to the grid (S_2 open), a synchronization method based on the flux vector orientation is used in order to avoid over current or an unstable operation in the connection instant.

During the synchronization the converter attempts to generate a three phase voltage system identical to the grid by aligning the flux vector ($\vec{\lambda_v}$) to the grid flux vector ($\vec{\lambda_g}$). This is done by orienting the q component of the grid flux to 0 through a PI regulator, thus obtaining a control angle and a vector whose d component is equal to the modulus of the grid flux. With these two references, the converter generates a flux vector identical to that of the grid, achieving a smooth connection to the system.

On the other hand, Fig. 3 shows the GFM control scheme implemented when the converter is already connected to the grid (S_2 closed). This control system is divided into three main blocks. The first one, highlighted in yellow in Fig. 3, is the Reactive Control Loop (RCL) and calculates the modulus of the reference flux, λ_v^*, as follows

$$\lambda_v^* = \lambda_{v0} + k_q(v^* - v) + \Delta\lambda_{v1} \tag{16}$$

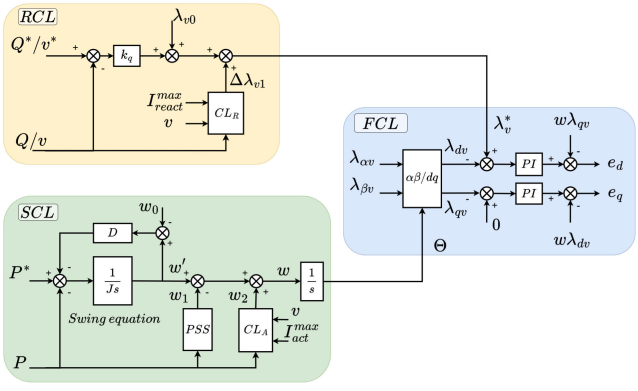

FIGURE 3. Flux vector control scheme.

This control loop can operate as PQ or PV node. In the laboratory it has been configured as a PV node, so the inputs are the measured voltage (v) at the converter's output and its reference (v^*), set to 1 p.u. The difference between the measurement and the reference is passed through a proportional regulator with gain k_q and the λ_{v0} term, which is also set to 1 p.u., is added. Thus, if the measured voltage v is lower than the reference voltage v^*, the modulus of the reference flux λ_v^* will increase. This causes the internal voltage of the converter e to also increase and in turn, the reactive power delivered by the converter, complying with (15). Finally, the $\Delta\lambda_{v1}$ term is added, which is the output of the reactive Current Limiter (CL_R) block shown in Fig. 4.

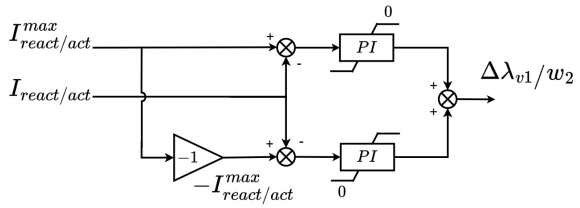

FIGURE 4. Reactive/Active current limiters.

The same Fig. 4 also shows the control scheme used to limit the active current, since its operation is similar but it will be explained below. This block is responsible for detecting whether the value of the reactive current is exceeding its maximum value and, if so, modifying the modulus of the calculated reference flux λ_v^* so it does not exceed the rated converter's current. First, the value of the measured reactive current is compared with its maximum (I_{react}^{max}) and minimum ($-I_{react}^{max}$) values. If the maximum value is exceeded, the value of the flux reference module is decreased, which causes the value of the injected current to decrease as well. Likewise, if the minimum value is exceeded, the value of the module is increased so that the reactive current is always within its limits.

At the bottom of Fig. 3 and highlighted in green is the Synchronization Control Loop (SCL). In order to obtain the w' term, the swing equation of a SG

$$P^* - P = J\frac{dw'}{dt} + D(w' - w_0) \tag{17}$$

has been replicated, where P and P^* are the active power measured and the active power reference respectively, D is the damping constant and J represents the virtual moment of inertia, defined as twice the inertia constant, H. The term w_1 is the output of a Power System Stabilizer (PSS) block which helps to compensate the damped active power response when the inertia constant is significant and the damping factor is low [50] and has the following transfer function

$$\frac{\Delta\overline{w_1}}{\Delta\overline{P}} = -K_w\frac{T_w s}{T_w s + 1} \tag{18}$$

where K_w is the gain and the T_w is the time constant.

Finally, w_2 is the output of the active Current Limiter (CL_A) block shown in Fig. 4, which is responsible for ensuring that the active current does not exceed its maximum value by operating in a similar way to the RCL but modifying the control angle. The maximum active current value has been calculated as follows

$$I_{act}^{max} = \sqrt{I_{max}^2 - I_{react}^2} \tag{19}$$

where I_{react} represents the reactive current measured at each moment and I_{max} the maximum current allowed by the converter, set to 1.1 p.u. Therefore, the more reactive current the converter is supplying, the lower the I_{act}^{max} value will be. With these terms, the control angle Θ can be obtained as

$$\Theta = \int w\,dt = \int w' - w_1 + w_2\,dt \tag{20}$$

The third and last control loop is the Flux Control Loop (FCL), highlighted in blue in Fig. 3. In this loop, in order to align the converter flux vector module with the d-axis, the λ_{dv} component is compared with the reference modulus λ_v^* obtained in the RCL block, and the λ_{qv} component is compared with 0. The error signals obtained are passed through two PI controllers. Finally, the cross-coupling terms are compensated by adding feedforward signals ($w\lambda_{dv}, w\lambda_{qv}$), obtaining the dq components of the reference voltages e_d, e_q.

Lastly, the inverse Park transformation ($dq-abc$) is applied to generate the three-phase voltage references (e_a, e_b, e_c). The switching pattern of the converter is then determined using space vector pulse width modulation (PWM) technique.

As a note it should be clarified that the control blocks shown in Fig. 2, Fig. 3 and Fig. 4 have been expressed in the Laplace domain, but in order to load the program into the control board it has been necessary to discretize it. The method used for the discretization of the blocks has been the Zero-Order Hold (ZOH) and the sample time, T_s, has been set at 384 µs, coinciding with the execution time of the converter control board.

For the regulators tuning, the method explained in [51] has been followed, where the stability of the system is also demonstrated by means of a small-signal analysis. According to Fig. 3 and if a X/R ratio is taken into account for the filter inductance, the transfer function of the plant can be defined as

$$G_P(s) = \frac{\lambda_{dv}}{e_d} = \frac{\lambda_{qv}}{e_q} = \frac{T_f}{T_f s + 1} \tag{21}$$

where T_f is the filter's time constant equal to L_f/R_f. Furthermore, the transfer function of the PI regulator can be expressed as:

$$G_R(s) = K_R\left(\frac{T_R s + 1}{T_R s}\right) \tag{22}$$

where T_R and K_R are the time and proportional constants respectively. Therefore, the open-loop transfer function can be expressed as

$$G(s) = G_R(s)G_P(s) = K_R\left(\frac{T_R s + 1}{T_R s}\right)\left(\frac{T_f}{T_f s + 1}\right) \tag{23}$$

Setting a T_R equal to T_f yields

$$G(s) = \frac{K_R}{s} \tag{24}$$

the closed-loop transfer function $G'(s)$ can then be obtained as

$$G'(s) = \frac{G(s)}{1 + G(s)} = \frac{K_R}{s + K_R} \tag{25}$$

Consequently, setting the K_R to 1 p.u. and the T_R equal to the T_f, a bandwidth equal to the nominal w is being set, leading to a stable system as demonstrated in [51].

V. EXPERIMENTAL RESULTS

This section presents the power test bed implemented, the National Grid requirements for GFM converters and the results obtained during the tests carried out in the laboratory. Data were collected using LabVIEW-based real-time monitoring and post-processed in Matlab. In addition, the grid emulator interface and oscilloscope have been used to obtain additional data in some tests. Due to actual power laboratory limitations, the converter has been configured with a nominal power of 10 kVA and a rated voltage of 120 V_{AC} instead of 230 V_{AC} in order to obtain currents with higher values. The other parameters used are given in the Appendix. The tests carried out according to National Grid's requirements have been: validation of the synchronization algorithm with the grid, current limitation, response to frequency changes, phase jumps and voltage dips and, finally, operation in islanded mode.

A. HARDWARE TEST BED DESCRIPTION

The components shown in Fig. 5 has been used in order to test the algorithm of the GFM based on the flux vector on a commercial converter according to the National Grid ESO requirements. These components are explained as follows.

- PV Emulator: Two Magna-Powers regulated DC power sources have been used to emulate the operation of a photovoltaic plant. Each source can supply 500 V and 20 A and, for these tests, they have been connected in parallel to obtain 500 V and 40 A. As they are unidirectional, protection diodes have been installed at the output of each source.
- VSC: The DC/AC converter consists of several important elements. The first of them is a control board which is composed of a DSP of the TIC6000 family of controllers programmable in C language from Matlab/Simulink. This board also has an ARM processor for the management of high speed communications, allowing

FIGURE 5. Test bed implemented.

UDP communication at 100 Mbit/sec of 64 variables for live visualization, which has been carried out on a PC with the LabVIEW tool. In addition, the control board also has a FPGA for the generation, supervision, protection and conditioning of both analog and digital inputs/outputs. The second element is the interface board, which is responsible for generating the control pulses and receiving the feedback pulses from the Insulated Gate Bipolar Transistors (IGBTs) drivers via an optical bus. In addition, the interface board contains the analog input channels and digital input/output channels. The converter also has the IGBTs and drivers, which are designed for total protection of the power system against malfunction. The switching frequency of the IGBTS, f_{sw}, is 2604 Hz. Finally, the VSC has a TM241CE40R PLC and a HMIGTO3510 HMI from Schneider and two switches, one for the AC side (S_2) and one for the DC bus (S_3), where a set of six 900 µF parallel capacitors addind up to 5.4 mF is installed.

- Filter: The filter of the converter is inside the cabinet and consists of a three-phase LC filter. The value of the inductances (L_f) is 200 µH and the value of the capacitors (C_f) is 200 µF. It should be noted that this filter is designed to operate at a nominal power of 300 kVA, but due to actual limitations of the laboratory, the converter has worked with a rated power of 10 kVA.
- AC Load: It is a three-phase resistive load adjustable from 0 to 10.5 kW if supplied at 230 V. The load has its own switch (S_4) to be able to connect or disconnect it to the power loop.
- Grid Emulator: The Pacific Power Source (PPS) 3450AZX has been used. This 45kW bi-directional source can operate as an AC or DC voltage source, AC or DC current source, or as a load. For the tests carried out, it has been configured as a three-phase AC voltage source, allowing through its interface to program frequency disturbances, phase jumps or voltage dips. In addition, the power source also has its own switch at the output (S_1).
- Transformers: Although not visible in Fig. 1, two 20 kVA transformers (T_1 and T_2), have been placed behind the equipment. Both transformers are Dyn11 type and have a transformation ratio of 400/230 V.

B. NATIONAL GRID REQUIREMENTS FOR GRID-FORMING CONVERTERS

The Best Practice Guide written by National Grid for Great Britain sets out the main requirements that a GFM model should include and how to validate its performance. These requirements are listed as follows.

- Reactive Capability: The converter should be able to absorb or produce Reactive Power range as specified in the Service Agreement.
- Voltage Control: Maintain the internal voltage phasor by controlling the angle and amplitude of the voltage modulated by the inverter independently of the grid voltage or the load.
- Active Power Control: The active power supplied by a GFM through controlled means of the positive phase sequence root mean square active power produced at fundamental system frequency by the control system of a GFM unit. Therefore, its behavior should replicate that of a synchronous generating unit with a traditional regulator coupled to its prime mover. In addition, it must be able to produce active power changes depending on the set point.
- Frequency Response: It is the injection or absorption of active power by a GFM plant to and from the system during a deviation of the system frequency away from the nominal frequency.
- PSS Tuning/Damping control: Control element that attempts to damp the power oscillations of the system. The validation of the PSS has not been carried out in the laboratory due to the complexity of the tests required, but it is something already validated by the same authors in another work through a Hardware in the Loop [50].
- Fault Ride Through and Fast Current Injection: The capability to be able to remain connected to the system and operate through periods of low voltage at the grid entry point caused by secured faults. In addition, fast reactive current injection is required.
- Active ROCOF Response Power: The active inertia power developed from a GFM plant plus the Active Frequency Response Power that can be supplied when subject to a rate of change of the system frequency.
- Active Phase Jump Power: The transient injection or absorption of active power from a GFM converter to the system as a result of changes in the phase angle between the internal voltage source of the GFM plant and the grid entry point.

C. SYNCHRONIZATION WITH THE GRID

Before any tests can be performed to validate the robustness of the proposed grid-forming control scheme, the converter must be connected to the grid. During this test, the first step for the converter is to detect that the DC bus is charged and then S_3 is closed. After that, if switch S_2 is open, the converter will start switching (t = 0.25 s) using the synchronization algorithm described above, generating flux components (λ_{dv}, λ_{qv}) equal to the grid (λ_d, λ_q), as shown in the first and third graphs of Fig. 6. This algorithm has a transient of about 0.25 s until the flux values reach their reference values. In the second and fourth plots of Fig. 6, the difference between λ_{dv} and λ_d noted as $error_d$ and the difference between λ_{qv} and λ_q noted as $error_q$ can be observed, becoming 0 in less than 0.5 s from the time the converter starts switching.

When the converter detects that its vector flux and the grid flux are synchronized, it activates the λ_{sinc} signal (t = 0.9 s). To ensure that both fluxes are properly synchronized before connecting to the grid, a counter is activated when the signal is active. If it is active for more than one second,

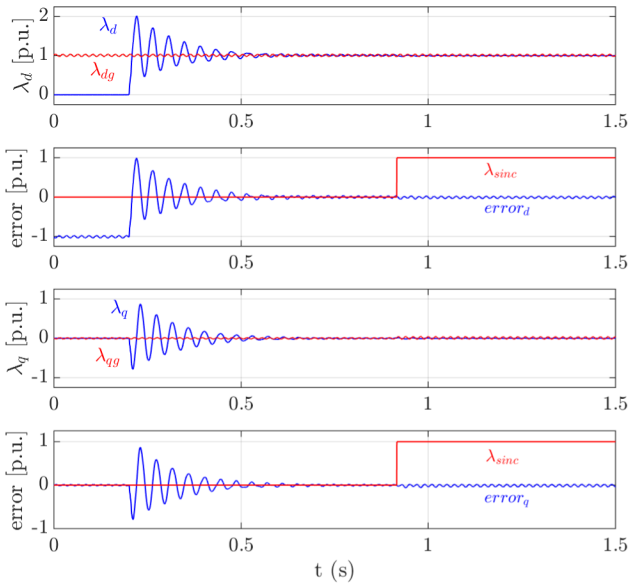

FIGURE 6. Fluxes *dq* components during synchronization.

it gives the command to close switch S_2 and change the synchronization algorithm to the SCL control, taking this process about 250 ms (t = 2.150 s). The second before proceeding to execute the circuit breaker closing maneuver has been placed as a preventive way, avoiding any failure in its connection and the tripping of the protections. Fig. 7 shows in the top graph a comparison between the phase A voltages of the converter and the grid before and after closing S_2 (t = 2.15 s), being practically identical. In the lower graph the instantaneous converter output currents are shown, where its peak at the moment of connection is very low.

D. ACTIVE CURRENT LIMITER

For this test, once the converter is connected to the grid, the active power reference (P_{ref}) of the SCL control loop has been varied by MODBUS communication. As can be seen in Fig. 8, at t = 8.5 s, the P_{ref} is set to a value of 0.4 p.u. At this point, the converter is able to perfectly follow the reference but the reactive power is increased as well

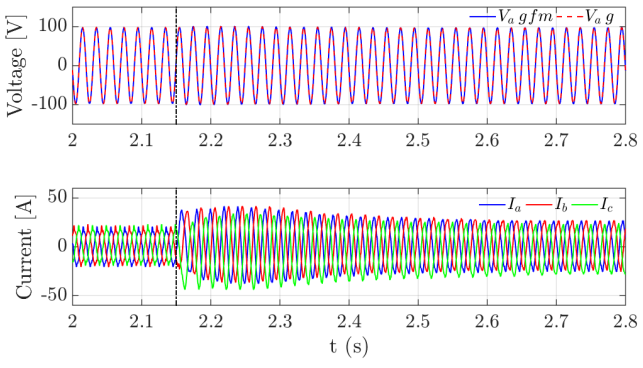

FIGURE 7. Voltage and currents during synchronization.

because the converter is configured as a PV node. At t = 11 s the P_{ref} value changes to 0.9 p.u. At this instant, the converter tries to reach the reference but, as the reactive current increases again, the maximum active current value calculated in (19) decreases. Therefore, the active current limiter starts to act, avoiding the converter to reach the set P_{ref} to prevent exceeding its maximum current value I_{max}, set to 1.1 p.u. This can be clearly seen in the lower graph, where I_{mod} represents the converter current module. The fact that the reactive power is proportionally so increased in the case of active power injections is due to the maximum current value used in the laboratory, set as 10% of the rated current of the commercial converter and by the PPS control itself. The active power variations cause a disturbance in the reactive power, but in case the converter maximum current was higher, these oscillations would be proportionally much lower than those that appear in these tests.

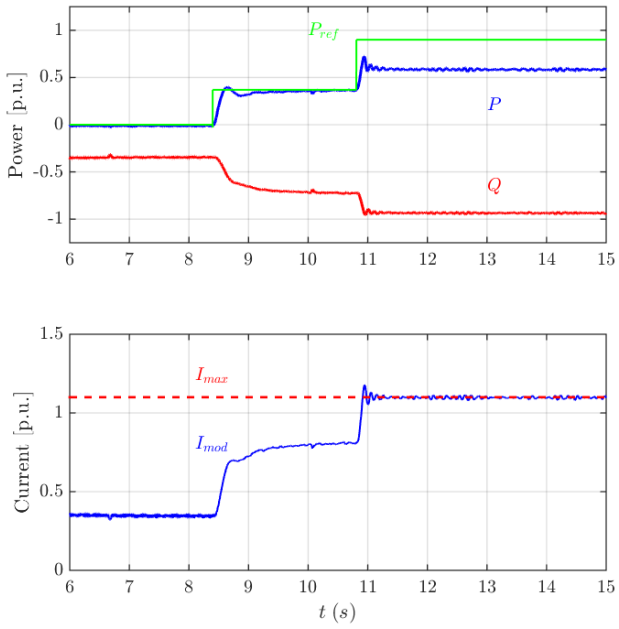

FIGURE 8. Active power reference, active and reactive power measurements and current module.

In addition, the same test has been replicated using a conventinal GFM converter control scheme [50] as shown in Fig. 9. This control is composed of one control loop for voltage (VC), one for current (CC) and a current limiter (CL) that consists of saturating the converter current reference module to its maximum value. The control angle used for the Park transformations is obtained from the SCL shown in Fig. 3 but without the current limiter included and the reference voltage v^* has been set to 1 p.u.

As illustrated in Fig. 10, the classical control (P_c, Q_c) performs similarly to the proposed method in the first part of the test with minor differences in dynamic response. However, when the converter needs to limit the current, the classical control becomes unstable, triggering the protection mechanisms to safeguard the equipment (t = 12.2 s).

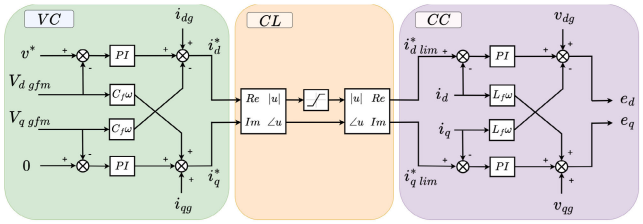

FIGURE 9. Classic GFM converter control scheme.

As explained in [32] and [52], this is because limiting the modulus of the converter's reference current can affect the converter's virtual power angle obtained through the synchronization loop, causing it to lose its synchronization with the grid and therefore its stability. Furthermore, although the P_{ref} can be controlled so that it never reaches a point that provokes current limiting, in the event of a voltage dip the same thing would happen with this control scheme. Therefore, for the following tests, replication with the classical control has been discarded.

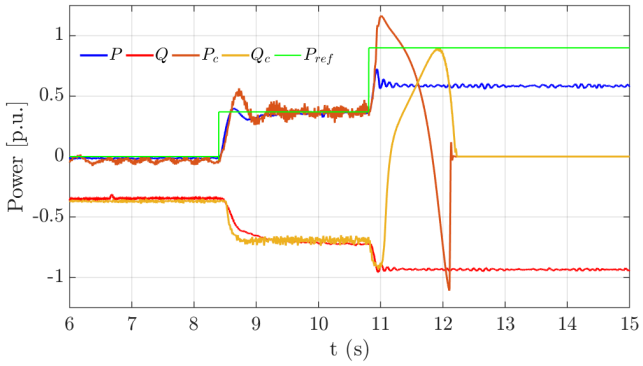

FIGURE 10. Comparison between flux vector and classic control schemes.

Finally, the dynamic differences between both control systems have been compared in Table 2. For this purpose, the active power of both tests has been analyzed between the instants t = 6 s and t = 10.5 s, since during this time, both systems are stable and undergo a set point change that allows a deeper analysis of their dynamics. The first column shows the steady-state error measured for both cases. As shown in Table 2 and Fig. 10, in steady state the classical control system has a slightly higher error. The second column measures the average error throughout this test, obtained as the difference between the reference power and the measured power. The classical GFM has a higher error in steady state and a greater oscillation when the reference changes, therefore the average error is also higher. Finally, the response of the flux vector based system is more damped and faster than that of the classical system, obtaining a lower settling time t_s fixed with a 5% error band.

E. FREQUENCY DISTURBANCE RESPONSE

During this test, a frequency variation of 0.5 Hz with a ROCOF of 1 Hz/s has been programmed into the grid via the PPS interface once the switch S_2 is closed. Fig. 11 shows

TABLE 2. Dynamics comparison between control schemes.

Control	$error$ (p.u.)	$\overline{error}$ (p.u.)	Power osc.	t_s (s)
Flux vector	0.01	0.0256	Damped response	0.6
Classic GFM	0.03	0.0451	Underdamped response	0.7

a comparison between the frequency calculated by the SCL loop, f, and the frequency measured by the grid emulator, f_g, in the first graph, the active and reactive powers in the second graph and the instantaneous currents measured at the converter output in the third graph. Finally, the voltage and current modulus of the converter are shown. When the frequency drop begins (t = 7.3 s), the converter starts to inject active power. As the constant D has been set to 50, for a variation of 1 % in the frequency the converter has to provide 50 % of its rated power in steady-state (P_d). As in the previous test, the active power injection provokes a modification in the voltage modulus. To counteract this effect since it is configured as a PV node, the converter starts absorbing reactive current, keeping the voltage modulus at 1 p.u. This causes the converter not to reach 50 % of its active power, since the limiter begins to act and only allows reaching 45 %. Thus, the maximum current set at 1.1 p.u. for the VSC is not exceeded. An oscillation can be seen in both the active power and the current modulus at t = 7.5 s, this is because

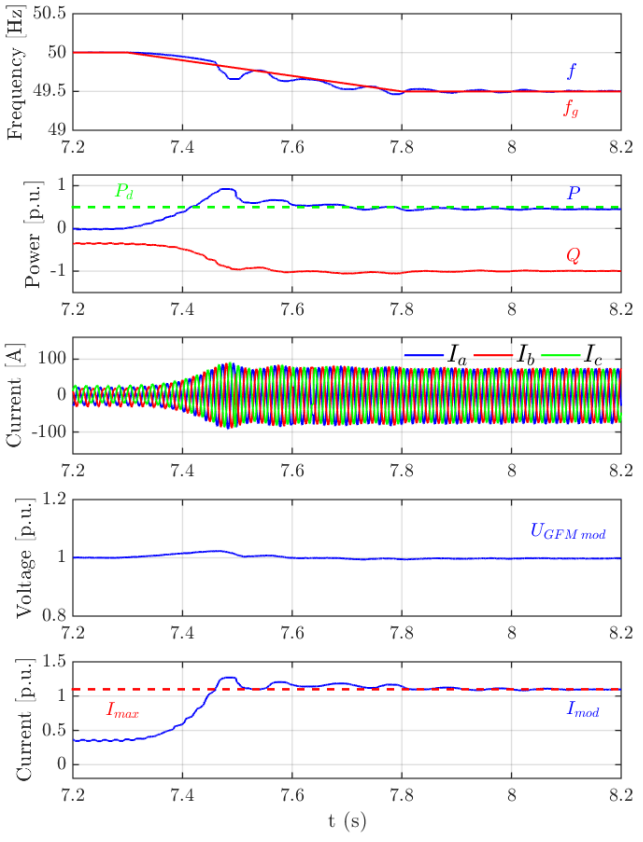

FIGURE 11. Frequency, active and reactive power, currents and voltage during a frequency disturbance.

the active current limiter starts to act on the control angle. As the Magna Power sources are unidirectional, it has not been possible to test a scenario in which a frequency increase occurs and the converter absorbs active power.

F. PHASE-JUMP RESPONSE

With the converter connected to the grid, a phase jump of 10° has been programmed through the PPS (t = 6.35 s). Fig. 12 shows the phasor representation of the grid voltages before and after the phase jump, respectively. This measurement has been obtained through the PPS interface. The top graph of Fig. 13 shows the SCL loop variable w, where the phase-jump is clearly visible. The active and reactive powers and the instantaneous currents are plotted in the middle and bottom graphs respectively. In this event the converter is able to maintain synchronism, also demonstrating its inertial response capability since a phase change means a frequency pulse. On the other hand, the reactive power is also affected but in a lesser extent, returning to its value once the system stabilizes. Since the phase jump occurs, it takes approximately 0.05 s for the converter to return to its previous operating state. In the results shown in [48] for a GFM converter, an identical response in power magnitude but of opposite sign can be seen. This is due to the fact that the phase jump provoked in the laboratory has been −10◦ instead of +10◦, since, in the second case the converter should absorb active power and, as explained above, it is not possible because the DC power sources are unidirectional.

G. LOW VOLTAGE RIDE-THROUGH AND REACTIVE CURRENT LIMITER

A three-phase voltage fault has been programmed in the PPS source to test the reactive current limiter and the Low Voltage Ride-Through strategy demanded by National Grid. The first and second plots of Fig. 14 shows the instantaneous voltages and currents of the converter. The third one shows how at t = 5.23 s, the voltage modulus ($U_{GFM\ mod}$) drops to 0.1 p.u. The last graph shows the active power P which remains at 0 during the entire fault and the reactive power Q which reaches its maximum value. For the input and output transitions of voltage faults a strategy has been implemented. The main reason is that the current limiters used have a disadvantage in that, in order to maintain stability, they do not limit the current module as other methods do but start operating when the current exceeds the maximum value. To protect the equipment, a power electronics blocking strategy is employed when an fast overcurrent is detected. Switching is blocked for few ms and then resumes its operation, injecting rapidly reactive current in order to try to recover the nominal voltage

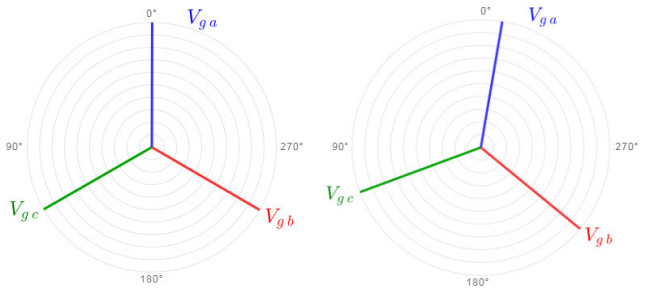

FIGURE 12. Phasor representation of the grid voltages before (left) and after (right) the phase jump.

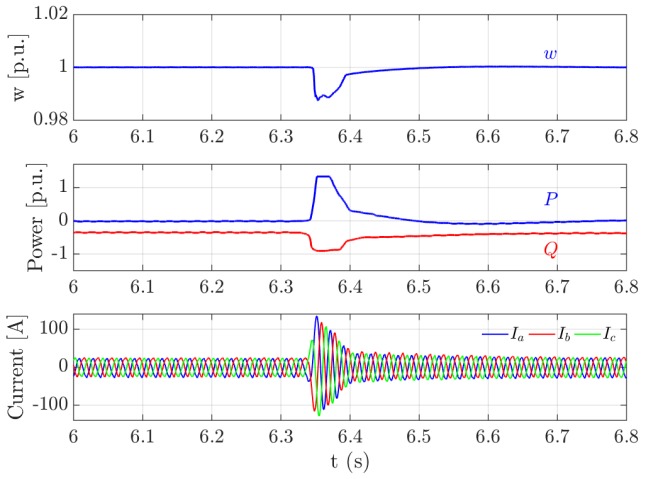

FIGURE 13. w, active and reactive power and currents during the phase jump.

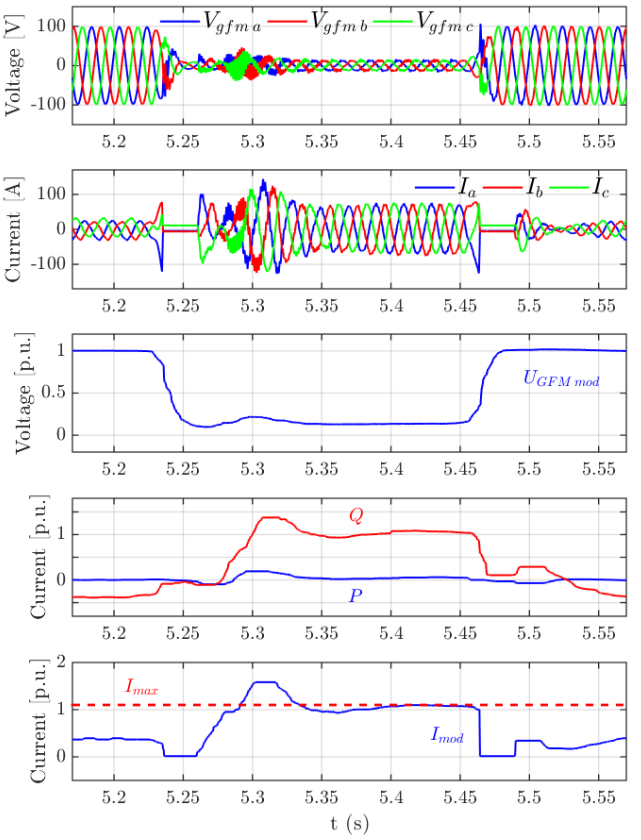

FIGURE 14. Voltage, current, active and reactive power during the voltage fault.

value until it reaches its maximum current value, set a 1.1 p.u as shown in the bottom graph. At this point, the limiter starts to act ensuring that this value is not exceeded. For the output of the voltage sag, the converter stops switching again, in case it detects an overcurrent, and then returns to its normal operating mode.

H. ISLANDED MODE

Finally, a transition of the converter from grid connected to islanded mode when the three-phase load is connected (S_4 closed) was tested. This test was carried out by opening switch S_1 suddenly (t = 4.65 s) once the converter is connected to the grid. The first graph of Fig. 15 shows how the frequency decreases about 0.1 % due to droop control and the value of the connected load and in the second graph shows that the voltage modulus of the converter remains constant, with almost no disturbances. In addition, Fig. 16 shows the instantaneous voltages and currents at the converter's output and the active and reactive powers measured in the next three graphs. When the converter starts to operate in islanded mode, its active and reactive powers increase. These oscillations of P and Q shown in this graph are those necessary to maintain voltage and frequency at their reference values while feeding the load. Lastly, Fig. 14 shows the instantaneous currents of phases A and B measured at the load with the oscilloscope.

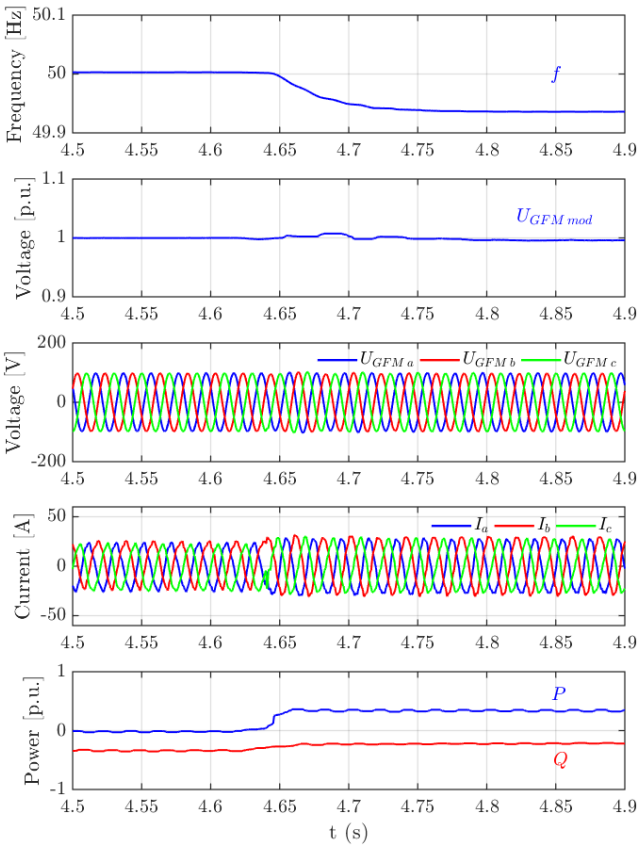

FIGURE 15. Frequency, voltage modulus, instantaneous voltages and currents and active and reactive powers during islanded mode.

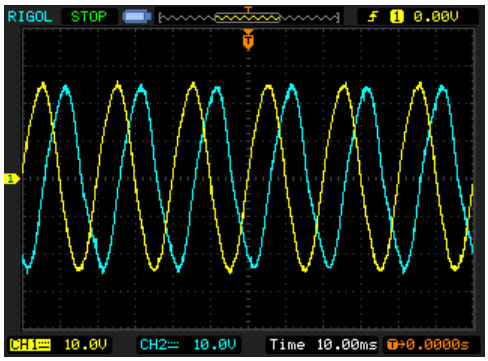

FIGURE 16. Phase A and B currents measured in the load during islanded mode.

TABLE 3. Test bed parameters.

Parameter	Value	Units
PV emulator voltage, V_{PV}	300	V
PV emulator current, V_{PV}	40	A
Converter rated power, S_n	10	kVA
Line to line VSC rated voltage (RMS)	120	V
Filter inductance, L_f	200	μH
Filter capacitance, C_f	200	μF
Nominal frequency, f_n	50	Hz
Switching frequency, f_{sw}	2604	Hz
T1 and T2 power rating	20	kVA
T1 and T2 rated line-line voltage primary	400	V
T1 and T2 rated line-line voltage secondary	230	V
Regulable three-phase load rated power (230V)	10.5	kW

TABLE 4. Control system parameters.

Parameter	Value	Units
Damping constant, D	50	p.u.
Inertia constant, H	0.25	s
PSS time constant, T_w	1.9197	s
PSS constant, K_w	0.026	p.u.
RCL gain, k_q	0.02	p.u.

Applying the oscilloscope conversion factor shows that the currents have a peak value of approximately 25 A, coinciding with those measured in the converter filter. The load, being adjustable, has been set to its maximum power which is 10.5 kW if fed at 230 V. As it is fed at 120 V, the value of its currents and the active power are lower.

VI. CONCLUSION

This paper proposes a novel scheme for commercial grid-forming converters based on the flux vector according to National Grid ESO requirements and for this purpose, provides an experimental validation in a power test bed. For this purpose, a power loop composed of the converter, PV and grid emulators and a three-phase load has been implemented. The results obtained show the robustness of this novel control system, allowing the grid-forming converters to operate in grid-connected as well as in islanded mode, a fundamental feature in distributed generation and to avoid blackouts from the grid. In addition, various tests have been carried out to demonstrate its ability to respond to frequency changes, phase

jumps or voltage sags with excellent dynamic performance. Finally, the correct operation of the novel current limiters proposed for this control scheme, which do not use internal current loops, has been verified. In addition, its performance has been compared with that of a classical control scheme for grid-forming converters showing a significant improvement in terms of stability.

As a future work, a control algorithm has to be designed in order that the converter is able to respond to unbalanced faults according to the latest grid codes.

APPENDIX

See Tables 3 and 4.

REFERENCES

[1] *Renewable Energy Statistics*, Int. Renew. Energy Agency (IRENA), Masdar City, United Arab Emirates, 2021.

[2] Q. Zhang, M. Mao, G. Ke, L. Zhou, and B. Xie, "Stability problems of PV inverter in weak grid: A review," *IET Power Electron.*, vol. 13, no. 11, pp. 2165–2174, Aug. 2020.

[3] S. F. Zarei, H. Mokhtari, M. A. Ghasemi, and F. Blaabjerg, "Reinforcing fault ride through capability of grid forming voltage source converters using an enhanced voltage control scheme," *IEEE Trans. Power Del.*, vol. 34, no. 5, pp. 1827–1842, Oct. 2019.

[4] *Stability Management in Power Electronics Dominated Systems: A Prerequisite to the Success of the Energy Transition*, ENTSO-E, Eur. Netw. Transmiss. Syst. Operators Electr. (Europe), Jun. 2022.

[5] R. Rosso, X. Wang, M. Liserre, X. Lu, and S. Engelken, "Grid-forming converters: Control approaches, grid-synchronization, and future trends—A review," *IEEE Open J. Ind. Appl.*, vol. 2, pp. 93–109, 2021.

[6] H. Wu and X. Wang, "Design-oriented transient stability analysis of PLL-synchronized voltage-source converters," *IEEE Trans. Power Electron.*, vol. 35, no. 4, pp. 3573–3589, Apr. 2020.

[7] J. Z. Zhou and A. M. Gole, "VSC transmission limitations imposed by AC system strength and AC impedance characteristics," in *Proc. 10th IET Int. Conf. AC DC Power Transmiss. (ACDC)*, Dec. 2012, pp. 1–6.

[8] National Grid ESO. (Jan. 2019). *Technical Report on the Events of 9 August 2019*. [Online]. Available: https://www.nationalgrideso.com/information-about-great-britains-energy-system-and-electricity-systemoperator-eso

[9] Australian Energy Market Operator. (Mar. 2017). *Black system South Australia 28 September 2016: Final Report*. [Online]. Available: https://apo.org.au/node/74886

[10] J. Matevosyan, J. MacDowell, N. Miller, B. Badrzadeh, D. Ramasubramanian, A. Isaacs, R. Quint, E. Quitmann, R. Pfeiffer, H. Urdal, T. Prevost, V. Vittal, D. Woodford, S. H. Huang, and J. O'Sullivan, "A future with inverter-based resources: Finding strength from traditional weakness," *IEEE Power Energy Mag.*, vol. 19, no. 6, pp. 18–28, Nov. 2021.

[11] *Minimum Specification Required for Provision of Virtual Synchronous Machine (VSM) Capability*, document GC0137, Nat. Grid ESO, 2019.

[12] R. Musca, A. Vasile, and G. Zizzo, "Grid-forming converters. A critical review of pilot projects and demonstrators," *Renew. Sustain. Energy Rev.*, vol. 165, Sep. 2022, Art. no. 112551.

[13] L. Zhang, L. Harnefors, and H.-P. Nee, "Power-synchronization control of grid-connected voltage-source converters," *IEEE Trans. Power Syst.*, vol. 25, no. 2, pp. 809–820, May 2010.

[14] S. Anttila, J. S. Döhler, J. G. Oliveira, and C. Boström, "Grid forming inverters: A review of the state of the art of key elements for microgrid operation," *Energies*, vol. 15, no. 15, p. 5517, Jul. 2022.

[15] P. Unruh, M. Nuschke, P. Strauß, and F. Welck, "Overview on grid-forming inverter control methods," *Energies*, vol. 13, no. 10, p. 2589, May 2020.

[16] W. Du, Z. Chen, K. P. Schneider, R. H. Lasseter, S. P. Nandanoori, F. K. Tuffner, and S. Kundu, "A comparative study of two widely used grid-forming droop controls on microgrid small-signal stability," *IEEE J. Emerg. Sel. Topics Power Electron.*, vol. 8, no. 2, pp. 963–975, Jun. 2020.

[17] M. A. Awal, H. Yu, S. Lukic, and I. Husain, "Droop and oscillator based grid-forming converter controls: A comparative performance analysis," *Frontiers Energy Res.*, vol. 8, pp. 168–183, Oct. 2020.

[18] S. Fazal, M. E. Haque, M. T. Arif, and A. Gargoom, "Droop control techniques for grid forming inverter," in *Proc. IEEE PES 14th Asia–Pacific Power Energy Eng. Conf. (APPEEC)*, Melbourne, QC, Australia, Nov. 2022, pp. 1–6.

[19] S. M. Mohiuddin and J. Qi, "A unified droop-free distributed secondary control for grid-following and grid-forming inverters in AC microgrids," in *Proc. IEEE Power Energy Soc. Gen. Meeting (PESGM)*, Montreal, QC, Canada, Aug. 2020, pp. 1–5.

[20] M. Ashabani and J. Jung, "Synchronous voltage controllers: Voltage-based emulation of synchronous machines for the integration of renewable energy sources," *IEEE Access*, vol. 8, pp. 49497–49508, 2020.

[21] M. Li, W. Huang, N. Tai, L. Yang, D. Duan, and Z. Ma, "A dual-adaptivity inertia control strategy for virtual synchronous generator," *IEEE Trans. Power Syst.*, vol. 35, no. 1, pp. 594–604, Jan. 2020.

[22] H. Bevrani, T. Ise, and Y. Miura, "Virtual synchronous generators: A survey and new perspectives," *Int. J. Electr. Power Energy Syst.*, vol. 54, pp. 244–254, Jan. 2014.

[23] M. Yu, A. J. Roscoe, C. D. Booth, A. Dysko, R. Ierna, J. Zhu, N. Grid, and H. Urdal, "Use of an inertia-less virtual synchronous machine within future power networks with high penetrations of converters," in *Proc. Power Syst. Comput. Conf. (PSCC)*, Genoa, Italy, Jun. 2016, pp. 1–7.

[24] D. Li, Q. Zhu, S. Lin, and X. Y. Bian, "A self-adaptive inertia and damping combination control of VSG to support frequency stability," *IEEE Trans. Energy Convers.*, vol. 32, no. 1, pp. 397–398, Mar. 2017.

[25] M. Colombino, D. Groß, J.-S. Brouillon, and F. Dörfler, "Global phase and magnitude synchronization of coupled oscillators with application to the control of grid-forming power inverters," *IEEE Trans. Autom. Control*, vol. 64, no. 11, pp. 4496–4511, Nov. 2019.

[26] B. B. Johnson, S. V. Dhople, A. O. Hamadeh, and P. T. Krein, "Synchronization of parallel single-phase inverters with virtual oscillator control," *IEEE Trans. Power Electron.*, vol. 29, no. 11, pp. 6124–6138, Nov. 2014.

[27] S. Azizi Aghdam and M. Agamy, "Virtual oscillator-based methods for grid-forming inverter control: A review," *IET Renew. Power Gener.*, vol. 16, no. 5, pp. 835–855, Apr. 2022.

[28] B. B. Johnson, M. Sinha, N. G. Ainsworth, F. Dörfler, and S. V. Dhople, "Synthesizing virtual oscillators to control islanded inverters," *IEEE Trans. Power Electron.*, vol. 31, no. 8, pp. 6002–6015, Aug. 2016.

[29] D. B. Rathnayake, M. Akrami, C. Phurailatpam, S. P. Me, S. Hadavi, G. Jayasinghe, S. Zabihi, and B. Bahrani, "Grid forming inverter modeling, control, and applications," *IEEE Access*, vol. 9, pp. 114781–114807, 2021.

[30] M. Zubiaga, C. Cardozo, T. Prevost, A. Sanchez-Ruiz, E. Olea, P. Izurza, S. H. Khan, and J. Arza, "Enhanced TVI for grid forming VSC under unbalanced faults," *Energies*, vol. 14, no. 19, p. 6168, Sep. 2021.

[31] J. C. Quispe and E. Orduña, "Transmission line protection challenges influenced by inverter-based resources: A review," *Protection Control Modern Power Syst.*, vol. 7, no. 1, pp. 3–17, Dec. 2022.

[32] L. Huang, H. Xin, Z. Wang, L. Zhang, K. Wu, and J. Hu, "Transient stability analysis and control design of droop-controlled voltage source converters considering current limitation," *IEEE Trans. Smart Grid*, vol. 10, no. 1, pp. 578–591, Jan. 2019.

[33] S. Jiang, Y. Zhu, T. Xu, and G. Konstantinou, "Current-synchronization control of grid-forming converters for fault current limiting and enhanced synchronization stability," *IEEE Trans. Power Electron.*, vol. 39, no. 5, pp. 5271–5285, May 2024.

[34] S. Jiang, T. Xu, and G. Konstantinou, "Current synchronization loop for enhanced fault tolerance and fast recovery in grid-forming converters," in *Proc. 49th Annu. Conf. IEEE Ind. Electron. Soc.*, Singapore, Oct. 2023, pp. 1–6.

[35] S. Mukherjee, P. Shamsi, and M. Ferdowsi, "Improved virtual inertia based control of a grid connected voltage source converter with fault ride-through ability," in *Proc. North Amer. Power Symp. (NAPS)*, Sep. 2016, pp. 1–5.

[36] K. O. Oureilidis and C. S. Demoulias, "A fault clearing method in converter-dominated microgrids with conventional protection means," *IEEE Trans. Power Electron.*, vol. 31, no. 6, pp. 4628–4640, Jun. 2016.

[37] K. Shi, W. Song, P. Xu, R. Liu, Z. Fang, and Y. Ji, "Low-voltage ride-through control strategy for a virtual synchronous generator based on smooth switching," *IEEE Access*, vol. 6, pp. 2703–2711, 2018.

[38] X. Lu, J. Wang, J. M. Guerrero, and D. Zhao, "Virtual-impedance-based fault current limiters for inverter dominated AC microgrids," *IEEE Trans. Smart Grid*, vol. 9, no. 3, pp. 1599–1612, May 2018.

[39] X. Wang, Y. W. Li, F. Blaabjerg, and P. C. Loh, "Virtual-impedance-based control for voltage-source and current-source converters," *IEEE Trans. Power Electron.*, vol. 30, no. 12, pp. 7019–7037, Dec. 2015.
[40] A. Gkountaras, S. Dieckerhoff, and T. Sezi, "Evaluation of current limiting methods for grid forming inverters in medium voltage microgrids," in *Proc. IEEE Energy Convers. Congr. Expo. (ECCE)*, Sep. 2015, pp. 1223–1230.
[41] D. Groß and F. Dörfler, "Projected grid-forming control for current-limiting of power converters," in *Proc. 57th Annu. Allerton Conf. Commun., Control, Comput. (Allerton)*, Monticello, IL, USA, Sep. 2019, pp. 326–333.
[42] F. Welck, D. Duckwitz, and C. Gloeckler, "Influence of virtual impedance on short circuit performance of virtual synchronous machines in the 9-bus system," in *Proc. Conf. Sustain. Energy Supply Energy Storage Syst.*, Sep. 2017, pp. 1–7.
[43] T. Qoria, H. Wu, X. Wang, and I. Colak, "Variable virtual impedance-based overcurrent protection for grid-forming inverters: Small-signal, large-signal analysis and improvement," *IEEE Trans. Smart Grid*, vol. 14, no. 5, pp. 3324–3336, Sep. 2023.
[44] J. Hu, J. Zhu, D. G. Dorrell, and J. M. Guerrero, "Virtual flux droop method—A new control strategy of inverters in microgrids," *IEEE Trans. Power Electron.*, vol. 29, no. 9, pp. 4704–4711, Sep. 2014.
[45] M. Malinowski, M. P. Kazmierkowski, S. Hansen, F. Blaabjerg, and G. D. Marques, "Virtual-flux-based direct power control of three-phase PWM rectifiers," *IEEE Trans. Ind. Appl.*, vol. 37, no. 4, pp. 1019–1027, Jul./Aug. 2001.
[46] Y. Cho and K.-B. Lee, "Virtual-flux-based predictive direct power control of three-phase PWM rectifiers with fast dynamic response," *IEEE Trans. Power Electron.*, vol. 31, no. 4, pp. 3348–3359, Apr. 2016.
[47] (Apr. 2023). *NGESO: Grid Forming Best Practice Grid*. Accessed: Jul. 3, 2024. [Online]. Available: https://www.nationalgrideso.com/document/278491/download
[48] *Minimum Specification Required for Provision of GB Grid Forming (GBGF) Capability*, document GC0137, NGESO, 2021.
[49] B. Fan, T. Liu, F. Zhao, H. Wu, and X. Wang, "A review of current-limiting control of grid-forming inverters under symmetrical disturbances," *IEEE Open J. Power Electron.*, vol. 3, pp. 955–969, 2022, doi: 10.1109/OJPEL.2022.3227507.
[50] J. Dolado, J. L. R. Amenedo, S. Arnaltes, and J. Eloy-Garcia, "Improving the inertial response of a grid-forming voltage source converter," *Electronics*, vol. 11, no. 15, p. 2303, Jul. 2022.
[51] J. D. Fernández, J. Eloy-García, E. R. Navarro, S. A. Gómez, and J. L. R. Amenedo, "Low-voltage ride-through algorithm for grid-forming converters," *IEEE Trans. Power Electron.*, vol. 40, no. 1, pp. 303–315, Jan. 2025, doi: 10.1109/TPEL.2024.3458193.
[52] H. Xin, L. Huang, L. Zhang, Z. Wang, and J. Hu, "Synchronous instability mechanism of P-f droop-controlled voltage source converter caused by current saturation," *IEEE Trans. Power Syst.*, vol. 31, no. 6, pp. 5206–5207, Nov. 2016.

JUAN DOLADO FERNÁNDEZ received the B.S. degree in electronic engineering and industrial automation from the University of Alcalá, in 2018, and the M.S. degree in automation and robotics from the University Polytechnic of Madrid, in 2020. He is currently pursuing the Ph.D. degree in electrical engineering with the University Carlos III of Madrid. His research interests include control of power electronic converters, grid-forming converters, and power system stability.

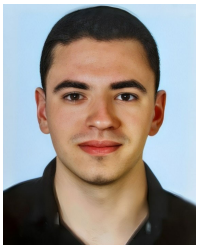

EDUARDO RAUSELL NAVARRO received the B.S. degree in electrical engineering from the Polytechnic University of Valencia, Spain, in 2021, and the M.S. degree in renewable energies and power systems from the University Carlos III of Madrid, Spain, in 2022, where he is currently pursuing the Ph.D. degree in electrical engineering. In 2024, he joined the Department of Technology, Research Centre for Energy, Environment, and Technology (CIEMAT), as a Researcher. His research interests include the control, modeling and simulation of power converters, renewable energy systems, energy storage systems, and green hydrogen systems.

JOSÉ LUIS RODRÍGUEZ AMENEDO (Senior Member, IEEE) received the M.S. degree in industrial engineering from the University Polytechnic of Madrid, in 1994, and the Dr.-Ing. (Ph.D.) degree in industrial engineering from the University Carlos III of Madrid, in 2000. From 1999 to 2000, he was with Iberdrola Engineering, as the Technology Wind Turbine Manager, and from 2001 to 2003 with Iberdrola Renewables as the Wind Energy Manager. In 2003, he joined the Electrical Department, University Carlos III of Madrid, as an Associate Professor. From 2008 to 2011, he requested an academic leave of absence for founding the technological companies Energy to Quality (E2Q) and Wind to Power Systems (W2PS). His research interests include renewable energy integration into the grids, power electronic converter control, HVdc transmission systems, and energy storage solutions.

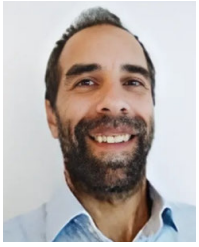

JOAQUÍN ELOY-GARCÍA received the Ph.D. degree in electrical engineering from the University Carlos III of Madrid, in 2007. He was with the University Carlos III of Madrid, until 2013. He is currently the Chief Technical Officer of IPS, a company of the Gransolar holding, focused on control of PV plants and storage plants.

SANTIAGO ARNALTES GÓMEZ received the Ph.D. degree in industrial engineering from the Polytechnical University of Madrid, in 1993. He is currently a Full Professor of electrical engineering with the University Carlos III of Madrid. His research interests include modeling, simulation, and control of renewable energy systems and energy storage systems.